

RESEARCH ARTICLE

10.1002/2015JC010840

Key Points:

- Langmuir turbulence deeply submerges microplastic marine debris
- Microplastic marine debris content is underestimated by surface measurements
- Sea state and rise velocity are key parameters for marine debris distributions

Correspondence to:

T. Kukulka,
kukulka@udel.edu

Citation:

Brunner, K., T. Kukulka, G. Proskurowski, and K. L. Law (2015), Passive buoyant tracers in the ocean surface boundary layer: 2. Observations and simulations of microplastic marine debris, *J. Geophys. Res. Oceans*, 120, 7559–7573, doi:10.1002/2015JC010840.

Received 16 MAR 2015

Accepted 24 OCT 2015

Accepted article online 30 OCT 2015

Published online 20 NOV 2015

Passive buoyant tracers in the ocean surface boundary layer: 2. Observations and simulations of microplastic marine debris

K. Brunner¹, T. Kukulka¹, G. Proskurowski^{2,3}, and K. L. Law²

¹School of Marine Science and Policy, College of Earth, Ocean, and Environment, University of Delaware, Newark, Delaware, USA, ²Sea Education Association, Woods Hole, Massachusetts, USA, ³School of Oceanography, University of Washington, Seattle, Washington, USA

Abstract This paper is the second of a two-part series that investigates passive buoyant tracers in the ocean surface boundary layer (OSBL). The first part examines the influence of equilibrium wind-waves on vertical tracer distributions, based on large eddy simulations (LESs) of the wave-averaged Navier-Stokes equation. Motivated by observations of buoyant microplastic marine debris (MPMD), this study applies the LES model and the parametric one-dimensional column model from part one to examine the vertical distributions of MPMD. MPMD is widely distributed in vast regions of the subtropical gyres and has emerged as a major open ocean pollutant whose distribution is subject to upper ocean turbulence. The models capture shear-driven turbulence, Langmuir turbulence (LT), and enhanced turbulent kinetic energy input due to breaking waves (BWs). Model results are only consistent with observations of MPMD profiles and the relationship between surface concentrations and wind speed if LT effects are included. Neither BW nor shear-driven turbulence is capable of deeply submerging MPMD, suggesting that the observed vertical MPMD distributions are a characteristic signature of wave-driven LT. Thus, this study demonstrates that LT substantially increases turbulent transport in the OSBL, resulting in deep submergence of buoyant tracers. The parametric model is applied to 11 years of observations in the North Atlantic and North Pacific subtropical gyres to show that surface measurements substantially underestimate MPMD concentrations by a factor of 3–13.

1. Introduction

This study is the second of a two part series that investigates passive buoyant tracers in the ocean surface boundary layer. The first part models the influence of idealized equilibrium wind-wave conditions on vertical tracer distributions [Kukulka and Brunner, 2015]. The second part applies the model to investigate observations of buoyant plastic marine debris, which has emerged as a major ocean pollutant.

Plastic marine debris has been a known ocean pollutant for several decades, but only recently have scientists started to study its widespread extent in all of our open oceans [Law *et al.*, 2010, 2014; Cozar *et al.*, 2014; Eriksen *et al.*, 2014]. Observations show that higher concentrations of plastic can be found in the subtropical gyres consistent with convergence of surface velocity fields due to Ekman transport [Law *et al.*, 2010], although additional geographic coverage and plastic content is not well known. The majority of the contamination found in the ocean is in the form of microplastic marine debris (MPMD), which forms as larger items fragment [Andrady, 2011]. The same chemically engineered properties that cause plastic to fragment rather than biodegrade also allow them to withstand harsh ocean environments and have long residency times [Andrady, 2011]. MPMD has many potentially adverse effects on marine life and their environment including effectively absorbing and transporting harmful chemicals [Mato *et al.*, 2001; Gold *et al.*, 2013], ingestion by marine life [Titmus and Hyrenbach, 2011; Davison and Asch, 2011; Laist, 1987; Thompson *et al.*, 2004], and transport of nonnative species to foreign waters [Teuten *et al.*, 2007; Teuten *et al.*, 2009].

A recent study found lower MPMD surface concentrations for higher wind speeds and MPMD concentrations at depths up to 20 m, indicating that wind-driven mixing submerges MPMD [Kukulka *et al.*, 2012b]. A comparison of subsurface observations to a simple one-dimensional column model that captures wind-driven mixing illustrates the mixing effect on vertical distributions of MPMD, but shows that the model substantially underestimates the observed concentration at greater depth [Kukulka *et al.*, 2012b]. By applying

our model from part one, this study addresses the hypothesis that wave-driven mixing results in the deep submergence of observed buoyant MPMD.

Langmuir turbulence (LT) results from the interaction between the turbulent current flow and the Stokes drift from surface waves [*Craik and Leibovich, 1976*]. The Stokes drift tilts vertical vorticity into the direction of wave propagation resulting in counter-rotating cells that are approximately aligned with the wind and wave direction [Leibovich, 1983; Thorpe, 2004; D'Asaro, 2014]. These cells can be up to several kilometers long and may extend vertically to the mixed layer depth. They lead to an alternating pattern of approximately parallel surface convergence and divergence zones known as "windrows" [Leibovich, 1983]. Bubbles, plastics, and other materials collect at the sea surface in these convergence zones associated with downwelling, which inject them deeper in the water column [Colbo and Li, 1999; Skillingstad, 2003; Harcourt and D'Asaro, 2010; Liang et al., 2011]. Large eddy simulations (LESs) are a common modeling technique used to study LT in the upper ocean [Skillingstad and Denbo, 1995; McWilliams et al., 1997]. Comparisons to various field observations show that LES successfully models the interaction between the turbulent current flow and surface waves by the Craik-Leibovich vortex force [Skillingstad et al., 1999; Gargett et al., 2004; Li et al., 2009; Kukulka et al., 2009, 2011, 2012a, 2013; Harcourt and D'Asaro, 2010].

Breaking waves (BWs) also contribute to wave-driven mixing by injecting turbulent kinetic energy (TKE) into the upper ocean [Terray et al., 1996]. Modeling BWs within LES is complicated due to their complex, unpredictable nature [e.g., Melville, 1996]. Noh et al. [2004] simulated the turbulence generated by BW in an LES model by imposing small-scale random surface forcing. Sullivan et al. [2007] represented BWs as stochastic resolved-scale accelerations and TKE injections. In part one of this study, we implemented a physically motivated BW model consistent with the previously utilized but significantly more complex BW models [Sullivan et al., 2007; McWilliams et al., 2012; Noh et al., 2004]. All of these LES studies are consistent with elevated TKE and TKE dissipation rates and increased mixing near the surface.

In this study, we investigate wave mixing effects on vertical distributions of observed MPMD using the models from part one. In the next section, we review MPMD observation data sets for the Atlantic and Pacific Oceans. Section 3 discusses the modeling framework with explicit wave effects. In section 4, we compare MPMD observations to simulations, before applying the model to estimate total (depth-integrated) MPMD content in section 5. Final conclusions on the importance of wave-driven mixing on MPMD distributions are presented in section 6.

2. Microplastic Marine Debris Observations

We analyze multiple data sets of surface concentrations and vertical profiles of MPMD obtained from Sea Education Association (SEA) [Law et al., 2010, 2014; Kukulka et al., 2012b] (Figure 1, top). SEA collected plastic debris using surface plankton net tows since the mid-1980s in the western Atlantic Ocean and since 2001 in the Pacific Ocean. A neuston net with a mouth size of 0.5 m by 1.0 m with a 335 μm mesh is towed at a ship speed of approximately 1 m/s for 30 min. As the net is towed across the surface, it collects marine biomass and any debris that accumulates on the surface to about 0.25 m depth. Plastic debris is then separated from the biomass and hand counted. The collected number of plastic pieces and tow volume, defined as the length of the tow multiplied by the width of the net, are used to compute plastic concentration in units of pieces per square km.

We use an 11 year subset of SEA surface plastic concentration observations; for North Atlantic Ocean expeditions from 2003 to 2010 between 22°N–38°N and 40°W–77°W [Law et al., 2010] and for North Pacific Ocean expeditions from 2002 to 2012 between 19°N–41°N and 118°W–177°W [Law et al., 2014], for a total of 708 surface observations (Figure 1, top). Each observation of surface plastic in this data set has a corresponding wind speed observation measured with a shipboard anemometer mounted on the top of the main mast, normalized to a standard 10 m reference height (U_{10}), and averaged over the duration of the net tow.

In contrast to the hundreds of SEA surface observations, we only have 13 subsurface plastic debris profiles from June to July 2010 in the Atlantic Ocean between 26°N–32°N latitude and 40°W–55°W [Kukulka et al., 2012b] and 8 subsurface profiles from October 2012 in the Pacific Ocean between 27°N–33°N and 136°W–147°W (pluses in top plots, Figure 1). Each of these profiles contains a surface observation from a neuston net tow, and at least one accompanying subsurface observation. The subsurface observations were made

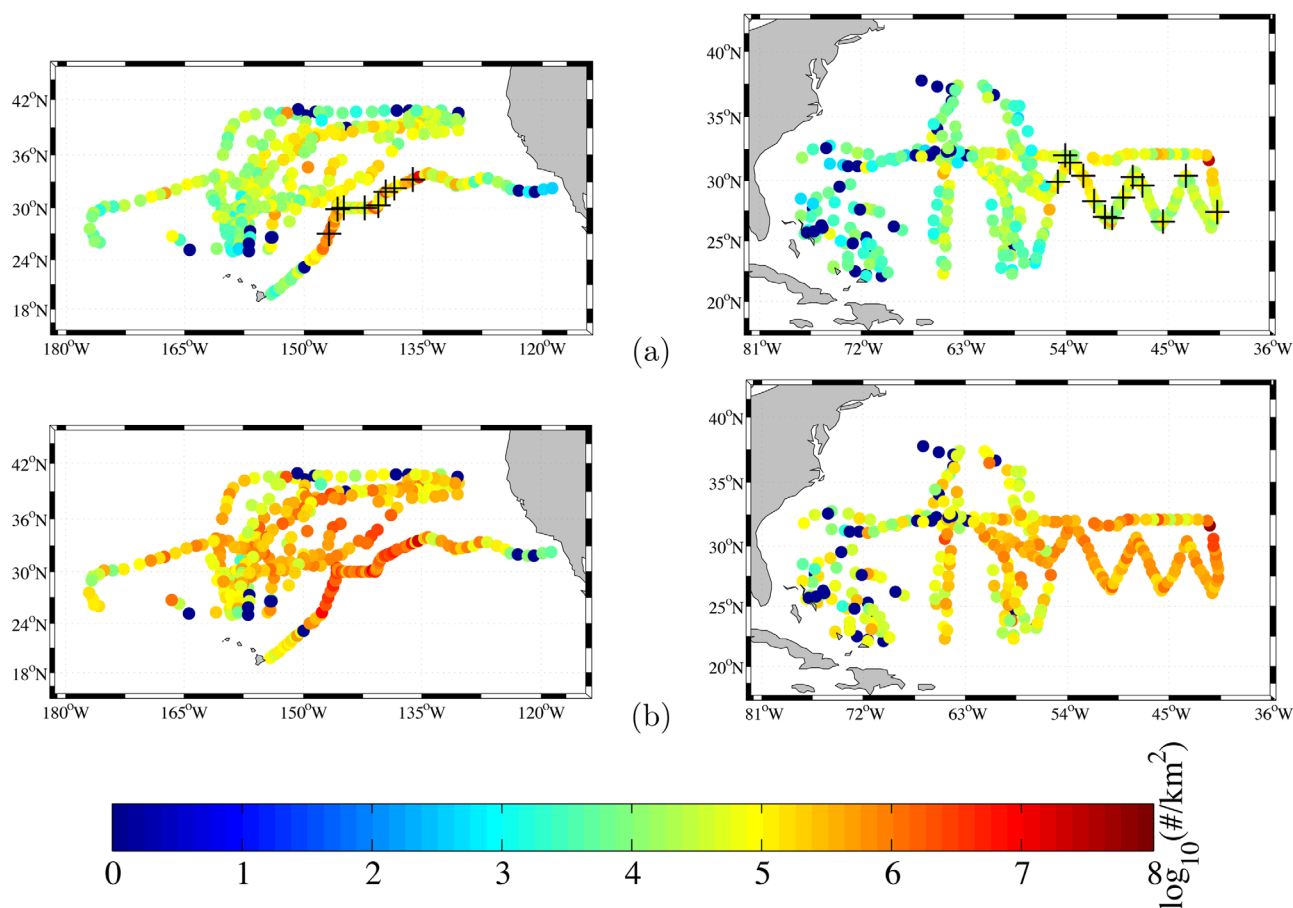


Figure 1. (a) Observed surface plastic concentration N_{totw} for the Atlantic and Pacific Oceans and (b) vertically integrated plastic concentrations N_{tot} , computed from the model representing typical conditions with the observed N_{totw} and measured wind speeds. The pluses in Figure 1a show profile locations.

using a modified Aquatic Research Instruments multiple-net Tucker Trawl [Hopkins *et al.*, 1973] (Atlantic profiles) and a custom-built Biological Environmental Sampling Systems Multiple Opening/Closing Net Environmental Sampling System (MOCNESS) net (Pacific profiles), both of which sample depth layers without contamination from casting or retrieving the net. Plastic concentration is expressed as number of plastic pieces collected per unit volume, with volume calculated from flowmeter and GPS data. The data set also includes wind speed measurements and the mixed layer depth for each profile, determined from a CTD cast based on a 0.2°C temperature change threshold [de Boyer Montegut *et al.*, 2004].

Laboratory experiments were conducted on a small subset of collected plastic pieces to measure the time each piece rose a set distance in a columnar fluid chamber filled with artificial seawater. These experiments gave a terminal buoyant rise velocity with mean and standard deviation of $w_b = 1.4 \pm 0.7 \text{ cm s}^{-1}$. This estimate of w_b is somewhat greater than, but still consistent with, the estimate from Reisser *et al.* [2015]. Plastic pieces with higher w_b are more likely to be surface trapped and have lower concentration at depth as downward turbulent mixing is not able to overcome the buoyant rise [Kukulka and Brunner, 2015]. As w_b decreases, the distribution of MPMD approaches vertical homogeneity. Better constraining the range of buoyant rise velocity through additional experiments is an important step for modeling MPMD concentration profiles.

3. Models of Passive Buoyant Tracers With Wave Effects

3.1. Large Eddy Simulations

We follow the approach from the part one study to model buoyant MPMD [Kukulka and Brunner, 2015]. We use the large eddy simulation (LES) model established by McWilliams *et al.* [1997], modified to capture enhanced TKE input due to BW and an idealized buoyant tracer. The LES code solves the Craik and Leibovich [1976] governing

momentum equation averaged over the subgrid scale to capture the Langmuir circulation dynamics by the Craik-Leibovich (CL) vortex force

$$\vec{F}_{CL} = \vec{u}_s \times \vec{\omega} \tag{1}$$

where \vec{u}_s is the Stokes drift vector and $\vec{\omega}$ is the vorticity vector. In part one, we specified \vec{u}_s for equilibrium wind-sea conditions by $\vec{u}_s = (u_{s,x}^w, 0, 0)$ with

$$u_{s,x}^w(z) = \frac{2}{g} \int_{-\infty}^0 \int_{-\pi}^{\pi} S(\sigma, \phi) \sigma^3 \exp\left[\frac{2\sigma^2 z}{g}\right] d\phi d\sigma \tag{2}$$

where g is gravitational acceleration, σ is the wave frequency, ϕ is the wave propagation direction, and z is the vertical coordinate. The x , y , and z components of a three-dimensional vector are in the wind, cross-wind, and upward directions, respectively. For all LES experiments, the Coriolis parameter is set to 10^{-4} s^{-1} . The wind-driven wave height spectrum S is parameterized based on the empirical spectrum from *Donelan et al.* [1985], which depends only on wind speed and wave age c_p^w/u_{*a} , where c_p^w is the peak phase speed for the wind-driven sea, and $u_{*a} = \sqrt{\tau/\rho_a}$ is the air-side friction velocity with air density ρ_a . For a given wind speed at 10 m height U_{10} , the wind stress τ is parameterized as $\tau = c_D \rho_a U_{10}^2$, where the drag coefficient c_D is from *Large and Pond* [1982].

The LES model also solves the transport equation of a passive buoyant tracer with constant buoyant rise velocity, w_b , in an Eulerian framework to study the effects of BW and LT on mixing a passive buoyant tracer, which acts as a proxy for MPMD.

3.2. Parametric Model

For equilibrium wind-sea conditions, LES results with wave effects of horizontally averaged concentration profiles of passive buoyant tracers $C(z)$ are compactly and accurately parameterized by

$$C(z) = C(0) \exp\left(\int_z^0 -\frac{w_b}{A(\xi)} d\xi\right) \tag{3}$$

where $A(z)$ is the eddy viscosity, which is constant near the sea surface and varies with depth below a transition depth z_T [Kukulka and Brunner, 2015]. For $|z| < z_T$, $A = A_0$ is given by

$$\frac{A_0}{u_* h} = \gamma_0^{bw} \frac{z_0}{h} + \gamma_{01} \exp\left(-\gamma_{02} \left[\frac{\lambda_p^w}{h}\right]\right) \frac{\lambda_p^w}{h} \tag{4}$$

where u_* is the water-side friction velocity (related to u_{*a} as $u_{*a} = u_* \sqrt{\rho_w/\rho_a}$ where ρ_w is the water density), h is the mixed layer depth, $z_0 = 0.5 \text{ m}$ is a hydrodynamic roughness length, λ_p^w is peak wavelength (related to c_p^w as $\lambda_p^w = 2\pi(c_p^w)^2/g$ using the linear dispersion relation for deep surface gravity waves), and γ_0^{bw} , γ_{01} , and γ_{02} are three empirical constants ($\gamma_0^{bw} = 1.60$, $\gamma_{01} = 0.145$, and $\gamma_{02} = 1.33$), which were estimated from LES results [Kukulka and Brunner, 2015]. For $|z| \geq z_T$, $A(z)$ has an assumed K profile parameterization (KPP) shape [Large et al., 1994]

$$A(z) = -w_* h \left(\frac{z}{h}\right) \left(1 + \frac{z}{h}\right)^2 \tag{5}$$

Following Kukulka and Brunner [2015], the turbulent velocity scale w_* is

$$\frac{w_*}{u_*} = \kappa + \gamma_{w1} \exp\left(-\gamma_{w2} \left[\frac{\lambda_p^w}{h}\right]\right) \frac{\lambda_p^w}{h} \tag{6}$$

where $\kappa = 0.4$ is the von Karman constant, and γ_{w1} and γ_{w2} are two additional empirical constants ($\gamma_{w1} = 2.49$ and $\gamma_{w2} = 0.333$). Without LT, $\lambda_p^w = 0$ and the model converges to the BW only solution for which mixing is enhanced only near the surface through the factor γ_0^{bw} relative to shear-driven turbulence. We recover the standard shear-driven turbulence (ST) solution when $\lambda_p^w = 0$ and $\gamma_0^{bw} = \kappa$ so that $A_0 = \kappa u_* z_0$ for $|z| < z_T$ and $A(z) \sim \kappa u_* |z|$ for $|z| > z_T$ but still close to the surface. The analytic model accurately parameterizes LES results for idealized equilibrium sea conditions and is computationally much more efficient than the LES model. Furthermore, it allows the investigation of combined or separate wave effects (BW only, LT only, BW and LT, or no wave effects).

3.3. Influence of Swell Waves on MPMD Distributions

Our previous LES studies have been conducted for idealized conditions with equilibrium seas and aligned wind-waves (i.e., wind and waves propagate in the same directions); however, open ocean conditions such as those for MPMD observations are commonly characterized by swell waves that are not in equilibrium with the local wind forcing [Hanley *et al.*, 2010; Semedo *et al.*, 2011]. Swell waves alter the Stokes drift of a wind-driven equilibrium sea [Webb and Fox-Kemper, 2011] and, therefore, affect the formation of Langmuir cells [Van Roekel *et al.*, 2012; Sullivan *et al.*, 2012; Kukulka *et al.*, 2013; McWilliams *et al.*, 2014; Rabe *et al.*, 2015].

A preliminary analysis of wave conditions and the swell influence on vertical distributions of MPMD indicates that our analytic solution captures, to leading order, typical wave conditions if a constant wave age for a fully developed sea is imposed in the model (Appendix A). However, extreme swell waves could modify the vertical distributions of MPMD, in particular, in low wind conditions. The occurrence of such extreme swell waves is unlikely and their detailed investigation left for future work.

4. Comparison of Observations and Simulations

4.1. LT Deeply Submerges MPMD

To investigate the influence of waves on the vertical distribution of MPMD, we apply our analytic solution (3) to observed profiles of the Atlantic (crosses, Figure 2) and Pacific (crosses, Figure 3) Oceans. We do not consider observation profiles with $U_{10} < 5 \text{ m s}^{-1}$ because turbulent mixing effects due to wind and waves are generally small, so that our model approach is not valid. The wind speed (to determine water-side friction velocity) and mixed layer depth is imposed for each modeled profile based on the observed conditions. Model solutions are shown for three different cases: (1) shear-driven turbulence only (ST solution, dash-dotted line), (2) breaking wave and shear-driven turbulence (BW solution, dashed line), and (3) combined Langmuir, breaking wave, and shear-driven turbulence (LT/BW solution, solid lines). For all wave solutions, the wave age is assumed constant at 35 (fully developed seas), based on a preliminary wave analysis for observed conditions (Appendix A). This leaves the surface concentration C_0 and buoyant rise velocity w_b as the only adjustable model parameters.

We first specify C_0 based on the surface observations and w_b based on the laboratory results. For the LT/BW model, we consider the mean $w_b = 1.4 \text{ cm/s}$, as well as plus and minus one standard deviation, i.e., $w_b = 2.1$ and 0.7 cm/s , respectively (three gray curves in Figures 2 and 3). The deepest submergence occurs for the smallest buoyant rise velocity of 0.7 cm/s and the largest surface trapping for the greatest $w_b = 2.1 \text{ cm/s}$. Without LT effects, we consider only the smallest $w_b = 0.7 \text{ cm/s}$ because surface trapping is much more pronounced, so that larger w_b would result in even greater surface trapping. Note that the BW solution for $w_b = 0.7 \text{ cm/s}$ is close to the LT/BW solution for $w_b = 2.1 \text{ cm/s}$, reflecting the strong control of LT on deeply submerging plastic pieces.

Observed plastic concentrations at depth are much closer to the LT/BW model solutions and usually fall in between those solutions for minimum and maximum buoyant rise velocity, signifying the importance of LT in MPMD transport to greater depth. Our results for the ST solution strongly suggest that without wave effects, deep submergence of MPMD could not occur, even with a relatively small buoyant rise velocity, so that MPMD would be mainly surface trapped, which is inconsistent with the observations. Note that some observations agree with both the BW solution for 0.7 cm/s and the LT/BW solution for 2.1 cm/s (e.g., Atlantic Station 085 in Figure 2 and Pacific Station 051 in Figure 3), which could be due to either swell suppressing turbulence or a relatively large w_b . This highlights the need for more complete measurements of waves and w_b in order to accurately quantify MPMD.

As expected, the largest concentrations at depth are found for profiles with the highest wind speeds when turbulent mixing is stronger (Stations 014 and 077 in Figure 2 and Station 069 in Figure 3). Observed profiles for Atlantic Station 077 and Pacific Station 069 are particularly striking examples for deep submergence that are consistent with our LT/BW solutions (see discussion below). Because of the limited number of observations and the variability in buoyant rise velocities and sea states, profiles do not display an obvious correlation between wind speed and concentration at depth as indicated, e.g., by Station 081 (Figure 2) and Station 035 (Figure 3). Some deep "outliers" exist even for the lowest w_b (e.g., Station 069 in Figure 3), meaning that the observed concentration is higher than the modeled concentration for those cases. In principle,

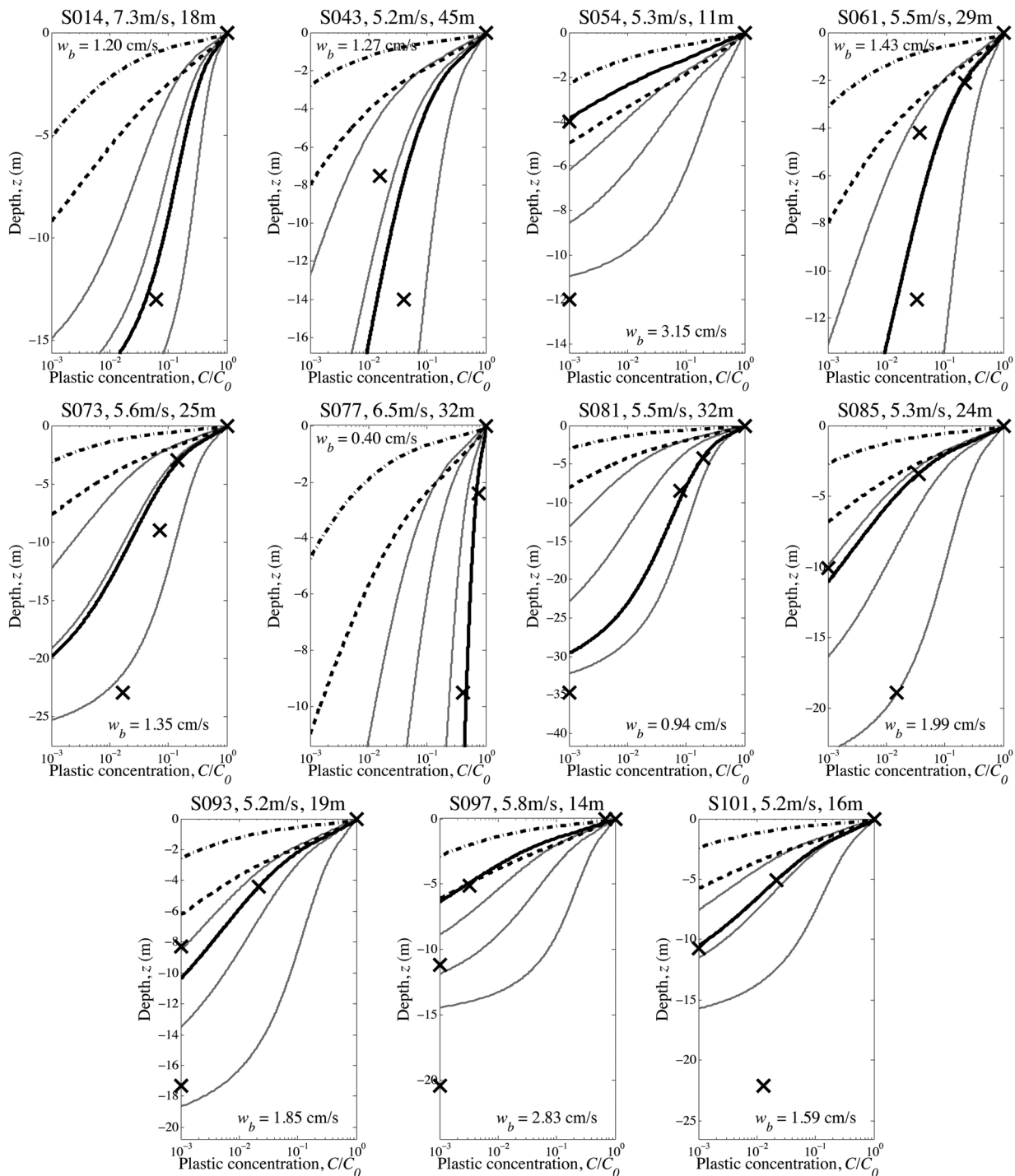


Figure 2. Comparisons of the Atlantic Ocean subsurface plastic observations (black crosses) and models using the observed surface concentrations C_0 for ST with $w_b = 0.7$ cm/s (dash-dotted line), BW with $w_b = 0.7$ cm/s (dashed line), and LT/BW with $w_b = 0.7, 1.4, 2.1$ cm/s (gray solid lines, deeper submergence for smaller w_b). The black line shows LT/BW solutions for which w_b and C_0 have been determined (w_b in legend) to match observations. For observed $C/C_0 < 10^{-3}$, we set $C/C_0 = 10^{-3}$. The title shows station name, U_{10} , and h , respectively.

the model can be improved to capture such deep outliers if multiple buoyant rise velocity classes are included in a single concentration profile solution. However, the small number of subsurface observations limits our ability to constrain a solution with multiple buoyant rise velocity classes.

Finally, we solve for C_0 and w_b by minimizing the sum of the weighted squared differences between the observed MPMD concentration profile and the LT/BW model solution (solid black curves in Figures 2 and 3).

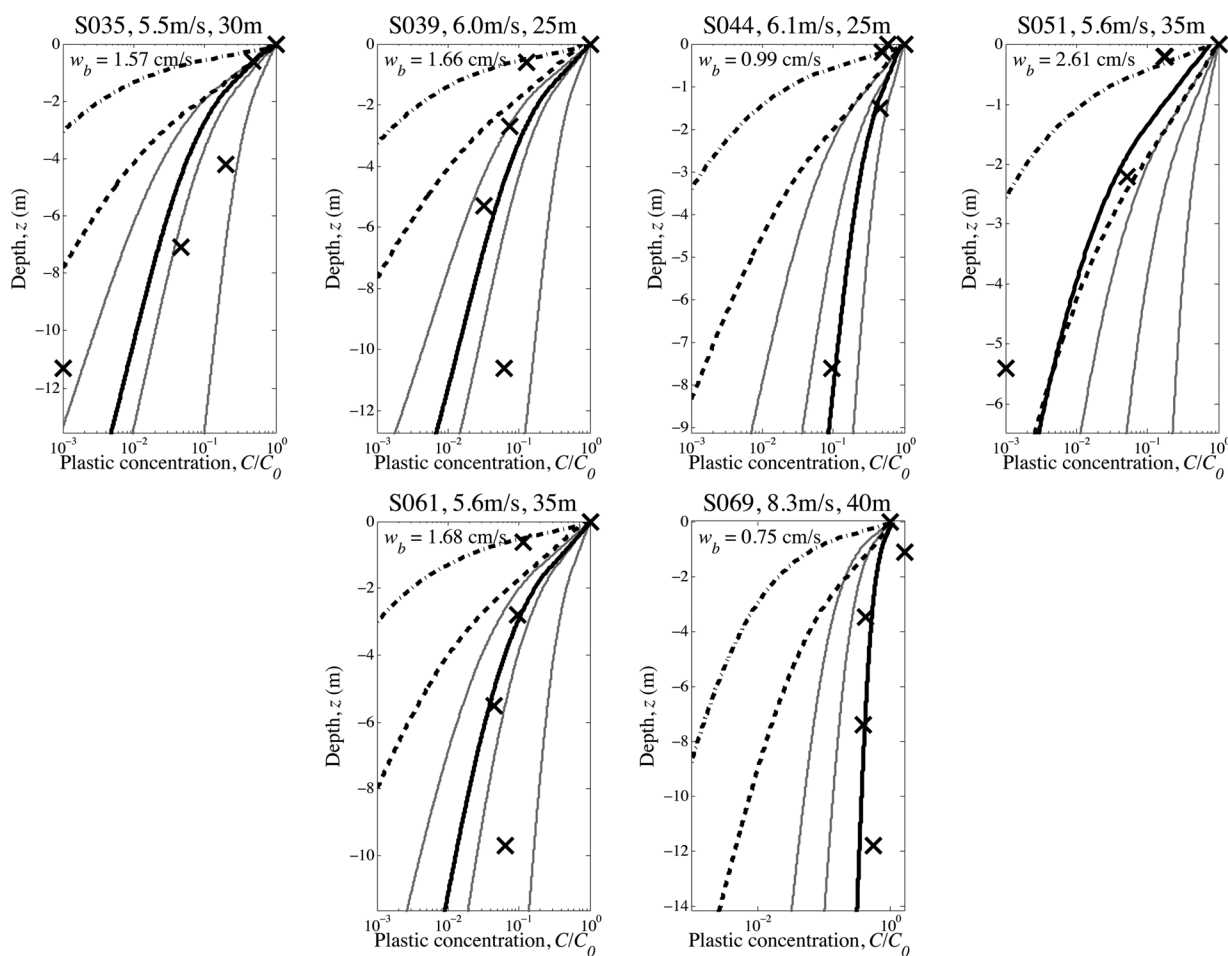


Figure 3. Comparisons of the Pacific Ocean subsurface plastic observations (black crosses) and models using the observed surface concentrations C_0 for ST with $w_b=0.7$ cm/s (dash-dotted line), BW with $w_b=0.7$ cm/s (dashed line), and LT/BW with $w_b=0.7, 1.4, 2.1$ cm/s (gray solid lines, deeper submergence for smaller w_b). The black line shows LT/BW solutions for which w_b and C_0 have been determined (w_b in legend) to match observations. For observed $C/C_0 < 10^{-3}$, we set $C/C_0=10^{-3}$. The title shows station name, U_{10} , and h , respectively.

For each profile measurement, the weights are determined by the number of plastic pieces, which are associated with a concentration estimate at depth, divided by the total number of plastic pieces in a profile. This weighting reflects that concentration estimates with a larger number of pieces are statistically more significant. We examine whether our w_b , obtained from a completely different approach, is consistent with the laboratory approach. Without LT effects, the buoyant rise velocity is substantially smaller than 0.7 cm/s, so that the ST and BW solutions are not consistent with the laboratory estimate of $w_b=1.4\pm 0.7$ cm/s. With LT effects, on the other hand, fitting the model C_0 and w_b to observations yields $w_b=1.7\pm 0.9$ cm/s for the Atlantic and $w_b=1.5\pm 0.8$ cm/s for the Pacific. These estimates of w_b are only consistent with laboratory observations if LT effects are included, confirming the importance of LT. Note that the relatively large standard deviation is only partially due to expected variability in w_b , but also captures erroneously variability in sea states during the observation period (Appendix A) since sea state is assumed constant in the model. This emphasizes the need for more accurate estimates of sea states to model MPMD. Overall, this comparison of observed and simulated MPMD highlights the importance of enhanced mixing due to wave-driven LT that is required to explain the observed submergence of buoyant plastic debris.

4.2. Relationship Between Wind Stress and Surface Concentration

The mixing effects of waves are wind stress dependent, so that surface concentration $N_{tow} = \int_{-0.25\text{m}}^0 C(z) dz$ depends on wind speed U_{10} (or u_*), where 0.25 m is the net tow depth. Consistent with the analysis for the Atlantic Ocean [Kukulka et al., 2012b], Pacific surface concentration observations also show that high plastic concentrations are more often measured at low wind speeds, while lower surface concentrations are associated with high wind speeds (Figure 4, left). Theory suggests that for fixed w_b and wave age, surface

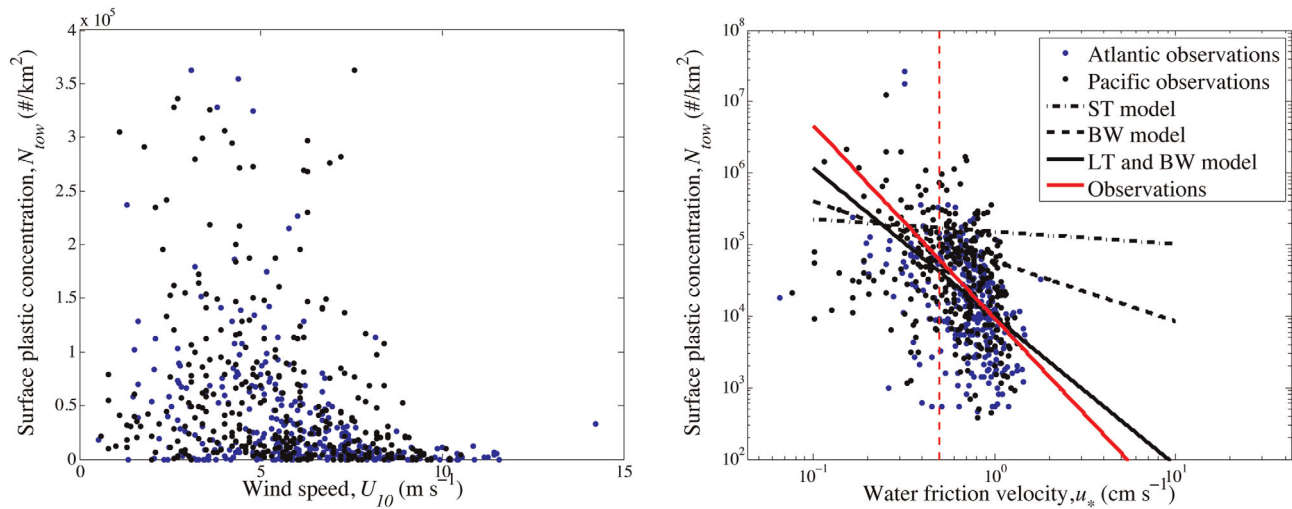


Figure 4. (left) Wind speed observed surface plastic concentration N_{tow} versus wind speed U_{10} and (right) water-side friction velocity u_* for the Atlantic (blue dots) and Pacific (black dots) Oceans. For $u_* > 0.5 \text{ cm s}^{-1}$ (dashed red line) wind effects are expected to be significant. Regression lines to the fit $N_{tow} = au_*^b$ for the observations (red) and ST (dash-dotted line), BW (dashed black line), and LT/BW solutions (solid black line) using $w_b = 1.4 \text{ cm s}^{-1}$. In the left plot, the 24 largest plastic concentration values greater than $4 \times 10^5 \text{ #/km}^2$ are not shown.

concentrations N_{tow} are inversely related to u_* , because greater u_* results in more mixing and reduced surface trapping for constant total MPMD content (Figure 5). Such an inverse relationship between u_* and surface concentration is observed despite scatter due to large spatial variability (dots on Figure 4, right). A linear regression analysis for the combined Atlantic and Pacific data sets for $u_* > 0.5 \text{ cm s}^{-1}$, when wind mixing effects are expected to be important, yields in an inverse relationship of $b = -2.7 \pm 0.6$ (95% confidence interval) for the regression model $N_{tow} = au_*^b$ (red line in right plot of Figure 4), which agrees with previous Atlantic results [Kukulka et al., 2012b]. All variables have been nondimensionalized by their respective units for the regression analysis, so that regression coefficients are nondimensional. Note also that there is

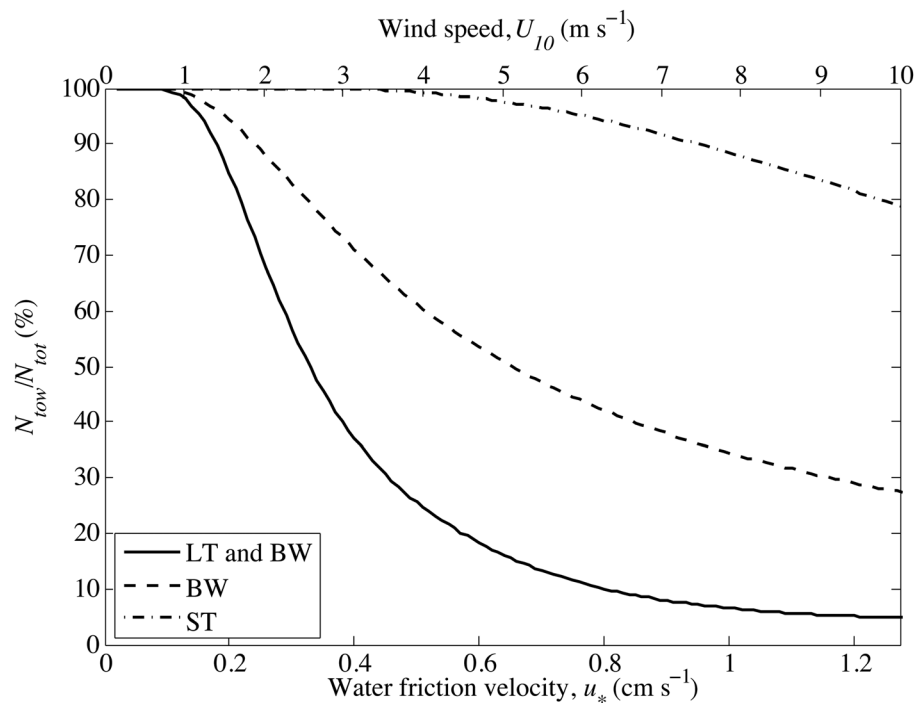


Figure 5. The fraction of total depth-integrated plastic concentration (N_{tot}) represented by the surface concentration (N_{tow}) as a function of water-side friction velocity u_* (or U_{10}) for the ST, BW, and LT/BW solutions with $w_b = 1.4 \text{ cm/s}$ and wave age 35.

Table 1. Increase Factors N_{tot}/N_{tow} for the Atlantic and Pacific Oceans^a

w_b (cm s ⁻¹)	Wave Effects	Atlantic Ocean		Pacific Ocean	
		Average	Max	Average	Max
0.7	LT and BW	8.2	88.8	13.3	79.9
	BW	2.9	16.1	3.3	10.8
	ST	1.3	5.7	1.4	3.4
1.4	LT and BW	3.7	40.7	5.3	34.6
	BW	1.7	6.8	1.9	4.9
	ST	1.2	2.1	1.3	1.6
2.1	LT and BW	2.4	21.1	3.3	17.3
	BW	1.4	4.4	1.5	3.3
	ST	1.2	1.5	1.2	1.4

^aThe increase is defined as the increase in the total plastic concentration from the surface concentration, averaged over all observations. Best estimates, based on comparisons between model solutions and observed profiles, are shown in bold.

$w_b = 1.4$ cm/s and $c_p/u_{*a} = 35$, the resulting regression coefficient is $b = -0.2$ for the ST solution (dash-dotted line in Figure 4), $b = -0.8$ for the BW solution (dashed line in right plot of Figure 4), and $b = -2.1$ for the LT/BW solution (solid line in right plot of Figure 4). For the empirical fit to the analytic model solutions, the 95% confidence intervals of b are over an order of magnitude smaller than $|b|$ and substantially smaller than for the observations. Therefore, only the LT/BW solution is consistent with the observed relationship between wind stress and surface concentration, highlighting again the need for LT dynamics to explain deep submergence of MPMD.

5. Estimate of Total Plastic Concentration

Maps of the surface observations from the Atlantic and Pacific Oceans (Figure 1, top) reveal large-scale spatial distribution patterns of MPMD. Higher concentrations of MPMD are found in the ocean gyres, consistent with wind-driven convergent surface flows associated with Ekman transport [Law et al., 2010, 2014]. We apply the buoyant tracer concentration model for different wave and buoyant rise velocity conditions to each surface observation, in order to estimate total upper ocean MPMD content $N_{tot} = \int_{-h}^0 C(z) dz$, i.e., volume concentrations integrated over the mixed layer. The wind stress is estimated from observed wind speeds, and the mixed layer depth is set constant at a typical value of $h = 30$ m, based on CTD profile observations.

The model solution is applied to obtain estimates of N_{tot} from measured N_{tow} and measured wind speeds. For the simulations, we use the LT/BW solution with $w_b = 1.4$ cm/s and $c_p/u_{*a} = 35$, representing typical conditions (Figure 1, bottom). The largest increase of total concentration occurs for observations with relatively low surface concentrations, because wind-driven mixing is usually enhanced for those cases. On average, N_{tot} exceeds N_{tow} by a factor of 3.7 for the Atlantic Ocean and 5.3 for the Pacific Ocean, with maximum increases by a factor of 40 and 34 for the Atlantic and Pacific Oceans, respectively (Table 1). These estimated values of N_{tot}/N_{tow} are greater than those from Kukulka et al. [2012b], because this study captures explicitly and more accurately the effects of deeply submerging LT.

To better understand the physical significance of wave-driven mixing, we also compute solutions for ST, BW, and LT/BW solutions and $w_b = 0.7, 1.4, 2.1$ cm/s (Table 1). BW effects alone nearly double the mean total plastic concentration estimates, even for relatively large w_b , with a maximum increase of 4 and 3 for the Atlantic and Pacific Oceans, respectively. The LT/BW solution for $w_b = 0.7$ cm/s, representing the largest solution, yields an increase in mean total concentration of 8.2 times the surface concentration for the Atlantic Ocean and 13 times the surface concentration for the Pacific Ocean. For particular net tows, N_{tot}/N_{tow} may increase by more than a factor of 88 and 79 for the Atlantic and Pacific Oceans, respectively (Table 1).

Estimates of N_{tot}/N_{tow} indicate that both buoyant rise velocity and wave-driven mixing have an important influence on the total plastic concentration (Table 1). As buoyant rise velocity decreases by 0.7 cm s⁻¹ from its mean value, the total concentration estimate approximately doubles (e.g., 3.7 with $w_b = 1.4$ cm s⁻¹ to 8.2 with $w_b = 0.7$ cm s⁻¹ for the Atlantic Ocean for LT/BW). The addition of LT also approximately doubles the total concentration estimate independent of buoyant rise velocity (e.g., 1.7 with BW only to 3.7 for LT/BW for the Atlantic Ocean with $w_b = 1.4$ cm s⁻¹). The increased total concentration (by a factor of 3 to 13

substantial scatter, e.g., due to the large spatial variability in plastic concentration, that is not explained by the simple empirical model.

To determine whether the ST, BW, or LT/BW solutions best fit the observations, we apply the same empirical regression analysis $N_{tow} = au_*^b$ to the analytic model. Note that b could alternatively be determined analytically from an asymptotic analysis of (3), but this is neither particularly straightforward nor physically insightful. With the default values,

times the observed surface concentration) resulting from the inclusion of wave-driven mixing indicates the substantial underestimation of total buoyant plastic concentration from surface measurements alone. Furthermore, our results suggest that accurate measurements of the sea state and buoyant rise velocity are key factors in further refining estimates of buoyant MPMD.

6. Conclusions

In this second part of a two-part investigation with focus on passive buoyant tracers in the ocean surface boundary layer, we compared simulations with observations of buoyant microplastic marine debris (MPMD) to determine the effect of wind and wave-driven mixing on vertical MPMD distributions. Simulations are based on the large eddy simulation (LES) and the parametric one-dimensional column model from part one [Kukulka and Brunner, 2015]. Both models capture wind-driven shear turbulence (ST), wave-driven Langmuir turbulence (LT), and enhanced turbulent kinetic energy input due to breaking waves (BWs). In order to investigate LT and BW effects, which can be imposed independently in the model, we analyzed solutions for only BW effects, combined LT and BW effects, and without any wave effects (ST solutions).

Model results of MPMD concentration are only consistent with observations if the effect of LT is included in the solution. Without LT effects, model solutions do not capture relatively high MPMD concentrations at greater depth. Furthermore, observations reveal an inverse relationship between wind stress and MPMD surface concentrations, indicating the importance of wind and wave-driven mixing. ST and BW-only solutions underestimate this surface mixing effect. Only the LT/BW solution is consistent with the observed relationship between wind stress and surface concentration, highlighting the importance of LT in deeply submerging MPMD. Therefore, our results suggest that observed MPMD distributions are a characteristic signature of wave-driven LT. This study demonstrates the importance of LT as a principle transport mechanism for buoyant tracers in the ocean surface boundary layer, resulting in their deep submergence.

It is important to keep in mind potential uncertainties and limitations of our approach. Although our analyses indicate that our model solutions are applicable to typical sea states, large swell waves may influence near-surface mixing, in particular, in the lowest wind conditions. Swell effects will be investigated more comprehensively in a future study. In addition, our analyses also highlight the need for more complete measurements of waves and buoyant rise velocity, in order to accurately quantify MPMD.

Finally, we have applied our model to surface MPMD observations [Law *et al.*, 2010, 2014] to estimate total (i.e., depth-integrated) MPMD concentration in the Atlantic and Pacific Oceans under different combinations of turbulent conditions and buoyant rise velocities. Model results reveal that total MPMD concentrations are substantially underestimated by surface measurements. On average, total MPMD concentrations increase by a factor of 3.7 times the surface concentration for the Atlantic Ocean and 5.3 times the surface concentration for the Pacific Ocean if mixing induced by LT and BW is accounted for. For particular net tows, the total MPMD concentration may increase by more than a factor of 88 and 79 relative to the surface estimate for the Atlantic and Pacific Oceans, respectively. These estimates of N_{tot}/N_{tow} are larger than those from Kukulka *et al.* [2012b], because this study captures explicitly the effects of deeply submerging LT. In order to make better estimates of total plastic concentration in the future, our results strongly suggest that we need more comprehensive observations of (a) buoyant rise velocity distributions to determine probability density functions, (b) two-dimensional wave height spectra, (c) wind vectors to estimate the wind-wave misalignment, and (d) plastic concentration at depth to constrain models. With improved estimates of the amount and vertical distribution of buoyant MPMD, we can better understand the impacts of this pollutant on the marine ecosystem.

Appendix A: Influence of Complex Wave Conditions on MPBD Distributions

In order to better understand uncertainties of the analytic model applied to observed MPMD, we assess realistic wind and wave conditions, including misaligned swell waves. Note that aligned means here that the misalignment angle between wind and wave propagation directions is zero. Misalignment refers to the significant misalignment angles with maximum misalignment for opposing wind and wave directions. We will first estimate the likely range of typical sea states to assess the applicability of our idealized model

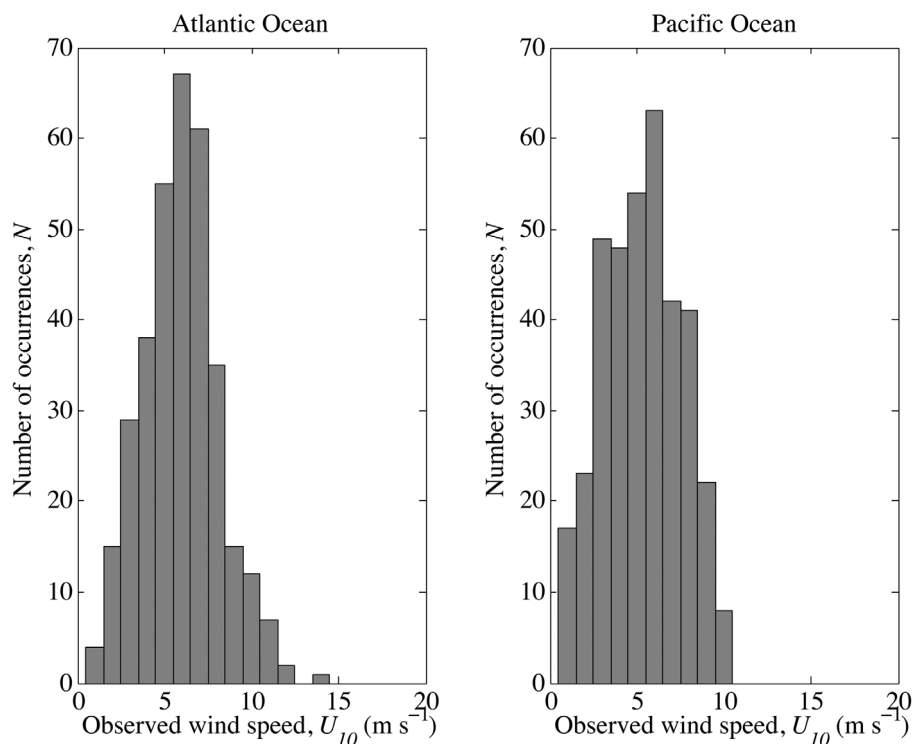


Figure 6. Comparison of histograms of the observed wind speed U_{10} for the (left) Atlantic and (right) Pacific Oceans subregions. The wind speeds are generally low, with the majority of observations falling between $U_{10} = 5$ and 10 m s^{-1} .

solutions during the observation period. The second goal of our wave analysis is to investigate some of the most extreme swell effects on buoyant tracer mixing in order to assess potential model uncertainties.

A1. Estimates of Typical Sea States

To estimate realistic wave properties such as wave age, direction of propagation, significant wave height, and peak period, we use NOAA’s archived WAVEWATCH III data [Tolman, 2009]. WAVEWATCH III is an ocean wave model that uses operational NCEP wind vectors as inputs to solve the random phase spectral action density balance equation for wave number-direction spectra and outputs two-dimensional wave height spectra [Tolman, 2009]. The wave model is run on a global and five regional nested grids. The regional models obtain boundary data hourly from the global model and each model is run 4 times daily for a 126 h forecast with 6 h hindcast to ensure continuity of swell conditions. The 70 arc min global grid (pre-2005) and 30 arc min global grid (post-2005) are used to obtain bulk spectral wavefield properties for the observation regions and time to complement the observational data to systematically assess wave-driven mixing effects.

Because there is substantial uncertainty associated with WAVEWATCH III predictions for complex swell seas for a particular instance and location, we choose a robust statistical analysis to characterize realistic sea states. This allows us to analyze a range of conditions that can be captured by the model and their implications for mixing. As a first step, WAVEWATCH III statistics are obtained for the Atlantic (between 22°N–38°N and 40°W–77°W) and Pacific (between 19°N–41°N and 118°W–177°W) Ocean observation regions and a single combined observation time period. The WAVEWATCH III data are extracted for each month in which observations were made. Statistical distributions are then obtained for the Atlantic and Pacific regions for all spatial and temporal data points. A preliminary analysis of wind and wave conditions indicates that statistics are not sensitive to different geographic subregions or time periods.

Observed wind speeds are fairly typical, nonstorm conditions (Figure 6). We focus on the wave parameters significant wave height h_s , peak period T_p , wave age c_p/u_{*a} where c_p is the peak phase speed, and the difference between wind and wave propagation direction, i.e., the wind-wave misalignment angle, θ for typical wind speeds between 5 and 10 m s^{-1} . We find that seas are relatively old and wind and waves are roughly aligned ($-45^\circ < \theta < 45^\circ$) approximately 50% of the time (Figure 7). This indicates that wavefields are either

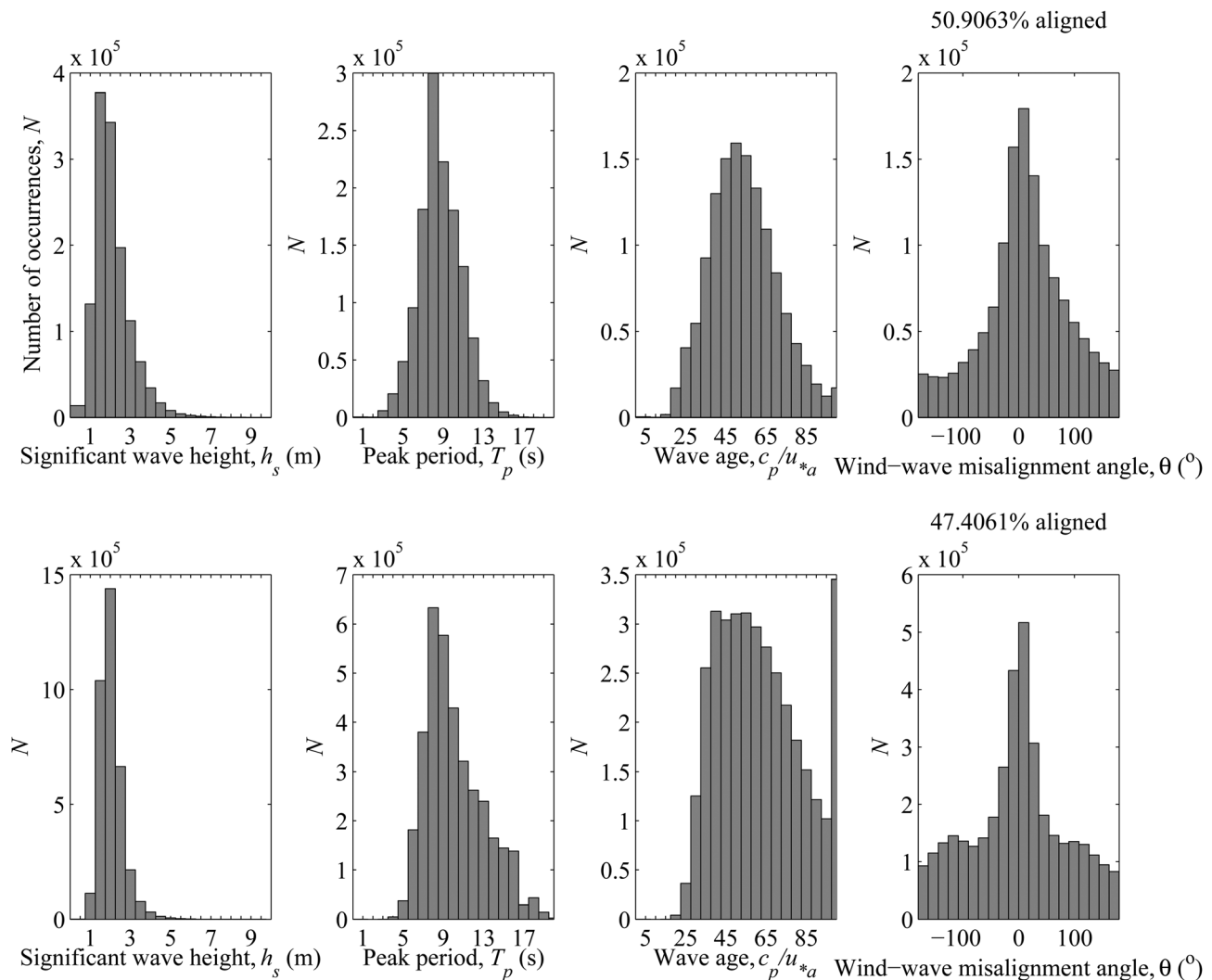


Figure 7. Comparison of histograms of the WAVEWATCH significant wave height h_s , peak period T_p , wave age c_p/u_{*a} , and wind-wave misalignment angle θ for the (top row) Atlantic and (bottom row) Pacific Ocean subregions (see main text) with $U_{10} = 5-10 \text{ m s}^{-1}$. Wave ages are relatively old and wind and waves are aligned approximately 50% of the time.

close to fully developed equilibrium wind seas or contain an important swell contribution. This is expected given the open ocean conditions with large fetch and relatively low wind speeds that allow surface waves to develop [Semedo *et al.*, 2011]. When wind and waves are approximately aligned, our model is approximately applicable (or mixing is even further enhanced, as discussed below) to the surface observations for a fully developed sea with wave age $c_p/u_{*a} = 35$ as this falls well within the previously identified range for which the parametric model accurately captures LES results with LT and BW effects.

A2. Estimates of Swell Stokes Drift

Previous studies indicate that swell waves which propagate along the wind enhance LT; whereas swell waves which propagate against the wind weaken LT [Van Roekel *et al.*, 2012; Sullivan *et al.*, 2012; Kukulka *et al.*, 2013; McWilliams *et al.*, 2014; Rabe *et al.*, 2015]. Based on our analysis of sea states, we estimate the influence of swell waves on the Stokes drift profile for typical and extreme swell waves that either propagate along or against the wind. If we assume that the wave height spectrum consists of a wind-driven part and a swell part, the Stokes drift vector can be decomposed into

$$\vec{u}_s = \vec{u}_s^w + \vec{u}_s^s \quad (\text{A1})$$

where \vec{u}_s^w is the wind-driven part and \vec{u}_s^s is the swell part. Assuming furthermore weak interactions between the swell and wind-sea wave spectra, $\vec{u}_s^w = (u_{s,x}^w, 0, 0)$ is given by (2) [McWilliams *et al.*, 2014]. The swell part

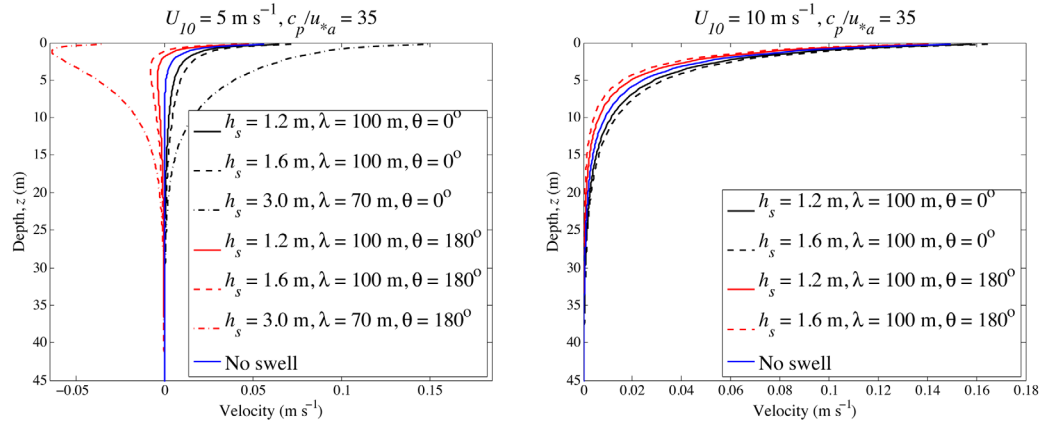


Figure 8. Comparison of the total Stokes drift velocity profiles for swell waves aligned (black lines) and 180° misaligned (red lines) with wind and waves with (left) $U_{10} = 5 \text{ m s}^{-1}$ and (right) $U_{10} = 10 \text{ m s}^{-1}$ and $\lambda_p^s = 100 \text{ m}$ ($T_p^s \approx 8 \text{ s}$). Stokes drift without swell (solid blue line) and extreme swell cases (dash-dotted lines) with $\lambda_p^s = 70 \text{ m}$ ($T_p^s \approx 7 \text{ s}$).

of the spectrum is represented by a monochromatic wave with period T_p^s , significant wave height h_s^s , and direction θ^s relative to the wind, so that

$$\vec{u}_s^s = u_s^s (\cos \theta^s, \sin \theta^s, 0) \quad (\text{A2})$$

where the swell Stokes drift magnitude is

$$u_s^s(z) = \frac{\pi^3 h_s^{s2}}{g T_p^{s3}} \exp\left(\frac{8\pi^2 z}{g T_p^{s2}}\right) \quad (\text{A3})$$

Consistent with (A1), the significant wave height has swell and wind-wave contributions

$$h_s^2 = h_s^{w2} + h_s^{s2} \quad (\text{A4})$$

where h_s^w is the equilibrium wind-sea component and h_s^s is the swell wave component. The equilibrium wind-sea component is estimated using the empirical formula [Moskowitz, 1964]

$$h_s^w = 0.24 U_{10}^2 / g \quad (\text{A5})$$

which is consistent with our wave spectrum for $c_p/u_{*a} = 35$ [Donelan *et al.*, 1985]. Using (A5) in (A4), we calculate the swell significant wave height for swell seas with $c_p/u_{*a} > 40$. Analysis of the wave and wind data suggests that the average swell significant wave height is $h_s^s = 1.2 \pm 0.4 \text{ m}$ (average plus and minus the standard deviation) for both the Atlantic and Pacific Oceans with peak periods, T_p , exceeding 8 s. As a first step to investigate typical conditions, we choose a small $T_p = 8 \text{ s}$, so that the resulting Stokes drift and its shear are relatively large and swell effects are likely overestimated since LT producing Stokes shear is more significant for this T_p . In order to understand an extreme swell effect, we also consider an unlikely extreme swell wave with $h_s = 3 \text{ m}$ and $T_p = 7 \text{ s}$, guided by the distributions from Figure 7.

Using (A1), the total Stokes drift velocity profile including swell waves aligned ($\theta = 0^\circ$) and misaligned ($\theta = 180^\circ$) with winds $U_{10} = 5, 10 \text{ m s}^{-1}$ and waves is plotted for expected ($h_s^s = 1.2, 1.6 \text{ m}$ and $\lambda_p^s = 100 \text{ m}$ or $T_p^s \approx 8 \text{ s}$) and extreme ($h_s^s = 3 \text{ m}$ and $\lambda_p^s = 70 \text{ m}$ or $T_p^s \approx 7 \text{ s}$) conditions (Figure 8). The angles of misalignment $\theta = 0^\circ$ and 180° are chosen as they represent the extreme limit of altering the wind-sea Stokes drift profile and, thus, influencing LT. Swell waves at higher wind speeds do not much alter the Stokes drift profile and are therefore unlikely to greatly affect LT and the mixing of a buoyant tracer (Figure 8, right). For $U_{10} = 5 \text{ m s}^{-1}$ and typical swell conditions, the Stokes drift shear is still strong even for misaligned cases at lower wind speeds, so realistic swell waves may not strongly affect the formation of LT and mixing (Figure 8, left). However, extreme swell waves alter the Stokes drift profile at lower wind speed so we expect them to affect mixing (Figure 8, left, dash-dotted lines).

A3. Swell Effects on Mixing

In order to understand the swell influence relative to equilibrium wind-wave conditions, we design LES experiments for aligned and misaligned ($\theta = 0, 180^\circ$, respectively) swell waves with $U_{10} = 5 \text{ m s}^{-1}$ and

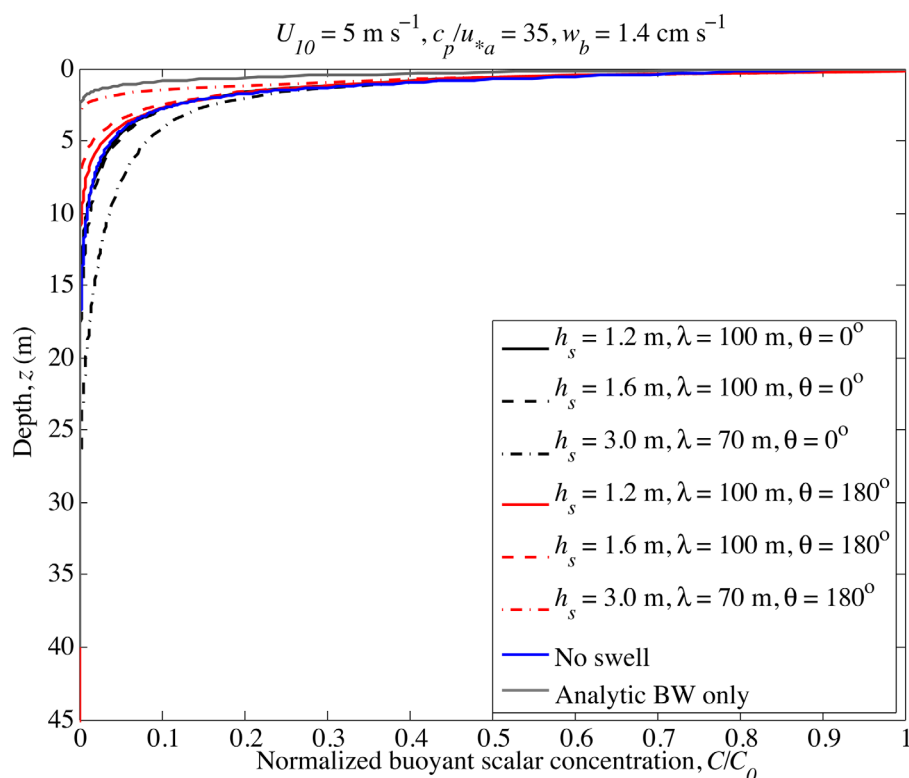


Figure 9. Comparison of the LES modeled results for the buoyant scalar concentration normalized by the surface concentration C_0 for average wind and wave conditions with the addition of realistic aligned and misaligned swell with $\lambda_p = 100$ m ($T_p \approx 8$ s) (solid and dashed black and red lines) and extreme aligned and misaligned swell with $\lambda_p = 70$ m ($T_p \approx 7$ s) (dash-dotted black and red lines), and no swell (solid blue line). The solid gray line is the analytic solution (3) with BW only ($\lambda_p^m = 0$).

compare concentration profile results to known parametric model solutions (3). Wind speed $U_{10} = 5 \text{ m s}^{-1}$ is chosen as we expect the swell to have a larger effect on mixing than for higher wind speeds. Realistic swell waves make very little difference in the amount of plastic contained at depth compared to the case without swell effects (Figure 9, blue line). However, the aligned extreme swell waves enhance deeper concentrations while the misaligned extreme swell wave significantly reduces the plastic concentration at depth. The misaligned extreme swell solution is close to the parametric BW only solution. The parametric solution for a fully developed sea with LT and BW is the most likely solution. Aligned swell waves only further increase the concentration at depth, so potentially plastics have an even higher concentration.

Acknowledgments

This work was supported by the U.S. National Science Foundation (grants OCE-1130678 and OCE-1352422), NOAA award NA10OAR4320148 Amendment 71, and the University of Delaware Research Foundation. We acknowledge computational and staff resources from IT at the University of Delaware. The data for this paper are available from the corresponding author Tobias Kukulka (kukulka@udel.edu).

References

- Andrady, A. (2011), Microplastics in the marine environment, *Mar. Pollut. Bull.*, *62*(8), 1596–1605.
- Colbo, K., and M. Li (1999), Parameterizing particle dispersion in Langmuir circulation, *J. Geophys. Res.*, *104*, 26,059–26,068.
- Cozar, A., et al. (2014), Plastic debris in the open ocean, *Proc. Natl. Acad. Sci. U. S. A.*, *111*(28), 10,239–10,244, doi:10.1073/pnas.1314705111.
- Craik, A., and S. Leibovich (1976), A rational model for Langmuir circulations, *J. Fluid Mech.*, *73*(3), 401–426.
- D'Asaro, E. A. (2014), Turbulence in the upper-ocean mixed layer, *Annu. Rev. Mar. Sci.*, *6*(1), 101–115, doi:10.1146/annurev-marine-010213-135138.
- Davison, P., and R. Asch (2011), Plastic ingestion by mesopelagic fishes in the North Pacific Subtropical Gyre, *Mar. Ecol. Prog. Ser.*, *432*, 173–180.
- de Boyer Montegut, C., G. Madec, A. Fischer, A. Lazar, and D. Iudicone (2004), Mixed layer depth over the global ocean: An examination of profile data and a profile-based climatology, *J. Geophys. Res.*, *109*, C12003, doi:10.1029/2004JC002378.
- Donelan, M., J. Hamilton, and W. Hui (1985), Directional spectra of wind-generated waves, *Philos. Trans. R. Soc. London A*, *315*, 509–562.
- Eriksen, M., L. C. M. Lebreton, H. S. Carson, M. Thiel, C. J. Moore, J. C. Borerro, F. Galgani, P. G. Ryan, and J. Reisser (2014), Plastic pollution in the worlds oceans: More than 5 trillion plastic pieces weighing over 250,000 tons afloat at sea, *PLoS ONE*, *9*(12), e111913, doi:10.1371/journal.pone.0111913.
- Gargett, A., J. Wells, A. Tejada-Martinez, and C. Grosch (2004), Langmuir supercells: A mechanism for sediment resuspension and transport in shallow seas, *Science*, *306*, 1925–1928.
- Gold, M., K. Mika, C. Horowitz, M. Herzog, and L. Leitner (2013), Stemming the tide of plastic marine litter: A global action agenda, *Pitzker Briefs*, *5*, 1–32.
- Hanley, K. E., S. E. Belcher, and P. P. Sullivan (2010), A global climatology of windwave interaction, *J. Phys. Oceanogr.*, *40*, 1263–1282, doi:10.1175/2010JPO4377.1.
- Harcourt, R., and E. D'Asaro (2010), Measurement of vertical kinetic energy and vertical velocity skewness in oceanic boundary layers by imperfectly lagrangian floats, *J. Atmos. Oceanic Technol.*, *27*, 1918–1935.

- Hopkins, T., R. Baird, and D. Milliken (1973), A messenger operated closing trawl, *Limnol. Oceanogr.*, *18*(3), 488–490.
- Kukulka, T., and K. Brunner (2015), Passive buoyant tracers in the ocean surface boundary layer: 1. Influence of equilibrium wind-waves on vertical distributions, *J. Geophys. Res. Oceans*, *120*, 3837–3858, doi:10.1002/2014JC010487.
- Kukulka, T., A. Plueddemann, T. Trowbridge, and P. Sullivan (2009), Significance of Langmuir circulation in upper ocean mixing: Comparison of observations and simulations, *Geophys. Res. Lett.*, *36*, L10603, doi:10.1029/2009GL037620.
- Kukulka, T., A. Plueddemann, J. Trowbridge, and P. Sullivan (2011), The influence of crosswind tidal currents on Langmuir circulation in a shallow ocean, *J. Geophys. Res.*, *116*, C08005, doi:10.1029/2011JC006971.
- Kukulka, T., A. Plueddemann, J. Trowbridge, and P. Sullivan (2012a), Nonlocal transport due to Langmuir circulation in a coastal ocean, *J. Geophys. Res.*, *117*, C12007, doi:10.1029/2012JC008340.
- Kukulka, T., G. Proskurowski, S. Morét-Ferguson, D. W. Meyer, and K. L. Law (2012b), The effect of wind mixing on the vertical distribution of buoyant plastic debris, *Geophys. Res. Lett.*, *39*, L07601, doi:10.1029/2012GL051116.
- Kukulka, T., A. Plueddemann, and P. Sullivan (2013), Inhibited upper ocean restratification in nonequilibrium swell conditions, *Geophys. Res. Lett.*, *40*, 1–5, doi:10.1002/grl.50708.
- Laist, D. (1987), Overview of the biological effects of lost and discarded plastic debris in the marine environment, *Mar. Pollut. Bull.*, *18*(6), 319–326.
- Large, W., and S. Pond (1982), Sensible and latent heat flux measurements over the ocean, *J. Phys. Oceanogr.*, *12*, 464–484.
- Large, W., J. McWilliams, and S. Doney (1994), Oceanic vertical mixing: A review and a model with nonlocal boundary layer parameterization, *Rev. Geophys.*, *32*(4), 363–403.
- Law, K. L., S. Morét-Ferguson, N. Maximenko, G. Proskurowski, E. Peacock, J. Hafner, and C. Reddy (2010), Plastic accumulation in the North Atlantic subtropical gyre, *Science*, *329*, 1185–1188.
- Law, K. L., S. Morét-Ferguson, D. Goodwin, E. Zettler, E. DeForce, T. Kukulka, and G. Proskurowski (2014), Distribution of surface plastic debris in the Eastern Pacific Ocean from an 11-year data set, *Environ. Sci. Technol.*, *48*, 4732–4738.
- Leibovich, S. (1983), The form and dynamics of Langmuir circulations, *Annu. Rev. Fluid Mech.*, *15*, 391–427.
- Li, M., S. Vagle, and D. Farmer (2009), Large eddy simulations of upper-ocean response to a midlatitude storm and comparison with observations, *J. Phys. Oceanogr.*, *39*, 2295–2309.
- Liang, J., J. McWilliams, P. Sullivan, and B. Baschek (2011), Modeling bubbles and dissolved gases in the ocean, *J. Geophys. Res. Oceans*, *116*, C03015, doi:10.1029/2010JC006579.
- Mato, Y., T. Isobe, H. Takada, H. Kanehiro, C. Ohtake, and T. Kaminuma (2001), Plastic Resin pellets as a transport medium for toxic chemicals in the marine environment, *Environ. Sci. Technol.*, *32*(2), 318–324.
- McWilliams, J., P. Sullivan, and C. Moeng (1997), Langmuir turbulence in the ocean, *J. Fluid Mech.*, *334*, 1–30.
- McWilliams, J., E. Huckle, J. Liang, and P. Sullivan (2012), The wavy Ekman layer: Langmuir circulations, breaking waves, and Reynolds stress, *J. Phys. Oceanogr.*, *42*, 1793–1816.
- McWilliams, J., E. Huckle, J. Liang, and P. Sullivan (2014), Langmuir turbulence in swell, *J. Phys. Oceanogr.*, *44*, 870–890.
- Melville, W. (1996), The role of surface-wave breaking in air-sea interaction, *Annu. Rev. Fluid Mech.*, *28*, 279–321.
- Moskowitz, L. (1964), Estimates of the power spectrums for fully developed seas for wind speeds of 20 to 40 knots, *J. Geophys. Res.*, *69*(24), 5161–5179.
- Noh, Y., H. S. Min, and S. Raasch (2004), Large eddy simulation of the mixed layer: The effects of wave breaking and Langmuir circulation, *J. Phys. Oceanogr.*, *34*, 720–735.
- Rabe, T., T. Kukulka, I. Ginis, T. Hara, B. Reichl, E. D'Asaro, R. Harcourt, and P. Sullivan (2015), Langmuir turbulence under Hurricane Gustav (2008), *J. Phys. Oceanogr.*, *45*(3), 657–677.
- Reisser, J., B. Slat, K. Noble, K. du Plessis, M. Epp, M. Proietti, J. de Sonnevile, T. Becker, and C. Pattiaratchi (2015), The vertical distribution of buoyant plastics at sea: An observational study in the north Atlantic gyre, *Biogeosciences*, *12*(4), 1249–1256, doi:10.5194/bg-12-1249-2015.
- Semedo, A., K. Sušelj, A. Rutgersson, and A. Sterl (2011), A global view on the wind sea and swell climate and variability from ERA-40, *J. Clim.*, *24*, 1461–1479.
- Skyllingstad, E. (2003), The effects of Langmuir circulation on buoyant particles, in *Handbook of Scaling Methods in Aquatic Ecology: Measurement, Analysis, Simulation*, edited by P. G. Strutton and L. Seuront, pp. 445–457, CRC Press, Boca Raton, Fla.
- Skyllingstad, E., and D. Denbo (1995), An ocean large eddy simulation of Langmuir circulations and convection in the surface mixed layer, *J. Geophys. Res.*, *100*(C5), 8501–8522.
- Skyllingstad, E., W. Smyth, J. Moun, and H. Wijesekera (1999), Upper-ocean turbulence during westerly wind burst: A comparison of large-eddy simulation results and microstructure measurements, *J. Phys. Oceanogr.*, *29*(1), 5–28.
- Sullivan, P., J. McWilliams, and W. Melville (2007), Surface gravity wave effects in the oceanic boundary layer: Large eddy simulation with vortex force and stochastic breakers, *J. Fluid Mech.*, *593*, 405–452.
- Sullivan, P., L. Romero, J. McWilliams, and W. Melville (2012), Transient evolution of Langmuir Turbulence in ocean boundary layers driven by hurricane winds and waves, *J. Phys. Oceanogr.*, *42*, 1959–1980.
- Terray, E., M. Donelan, Y. Agrawal, W. Drennan, K. Kahma, A. Williams, P. Hwang, and S. Kitaigorodskii (1996), Estimates of kinetic energy dissipation under breaking waves, *J. Phys. Oceanogr.*, *26*, 792–807.
- Teuten, E., S. Rowland, T. Galloway, and R. Thompson (2007), Potential for plastics to transport hydrophobic contaminants, *Environ. Sci. Technol.*, *41*(22), 7759–7769.
- Teuten, E., et al. (2009), Transport and release of chemicals from plastics to the environment and to wildlife, *Philos. Trans. R. Soc. B*, *364*(1526), 2027–2045.
- Thompson, R., Y. Olsen, R. Mitchell, A. Davis, S. Rowland, A. John, D. McGonigle, and A. Russell (2004), Lost at sea: Where is all the plastic?, *Science*, *304*(5672), 838.
- Thorpe, S. (2004), Langmuir circulation, *Annu. Rev. Fluid Mech.*, *36*, 55–79.
- Titmus, A., and D. Hyrenbach (2011), Habitat associations of floating debris and marine birds in the north east Pacific Ocean at coarse and meso spatial scales, *Mar. Pollut. Bull.*, *62*(11), 2496–2506.
- Tolman, H. (2009), User manual and system documentation of WAVEWATCH-III version 3.14, *Tech. Note 276*, NOAA/NWS/NCEP/MMAB, Camp Springs, Md.
- Van Roekel, L., B. Fox-Kemper, P. Sullivan, P. Hamlington, and S. Haney (2012), The form and orientation of Langmuir cells for misaligned winds and waves, *J. Geophys. Res.*, *117*(C5), 1978–2012.
- Webb, A., and B. Fox-Kemper (2011), Wave spectral moments and Stokes drift estimation, *Ocean Modell.*, *40*(3–4), 273–288, doi:10.1016/j.ocemod.2011.08.007.